The energetics of heterogeneous deformation in open-cell solid foams

Gustavo Gioia[1], Yu Wang[2] & Alberto M. Cuitiño[2]

26 June 2000

Compressed open-cell solid foams frequently exhibit spatially heterogeneous distributions of local stretch. The theoretical aspects of this deformation habit have not been clearly elucidated. Here we propose a simple nonlinear model aimed at illustrating the most salient features of the micromechanics of uniaxially stretched solid foams. Then we study the energetics of the model to show that the stretch heterogeneity observed in experiments stems from the nonconvexity of the governing energy functional, which favors two characteristic values of local stretch. These characteristic values are independent of the applied overall stretch, and define two configurational phases of the foam. The predicted stretch distributions correspond to stratified mixtures of the phases; stretching occurs in the form of a phase transformation, by growth of one of the phases at the expense of the other. We also compare the predicted mechanical response with experimental data for a series of foams of different densities, and discuss the analogy between the stretching of foams and the liquefaction of van der Waals gases. Lastly, we perform displacement field measurements using the digital image correlation technique, and find the results to be in agreement with our predictions.

1 Introduction

Solid foams are light materials which are employed in numerous engineering applications. In packaging, for example, polymeric solid foams are very effective at shielding fragile products from the jolts associated with transportation and handling. In the aeronautical industry, polymeric foams and honeycombs are the most commonly used materials in the cores of sandwich panels. Closer to everyday life, many food stuffs happen to be solid foams, too; in fact, most research into the behavior of brittle solid foams has been aimed at characterizing the "crunchiness" of snacks and crackers. Solid foams also occur in the form of natural materials, among which cancellous bone has elicited perhaps the most interest.

[1]Department of Theoretical and Applied Mechanics, University of Illinois, Urbana, IL 61801.
[2]Department of Mechanical and Aerospace Engineering, Rutgers University, Piscataway, NJ 08854.

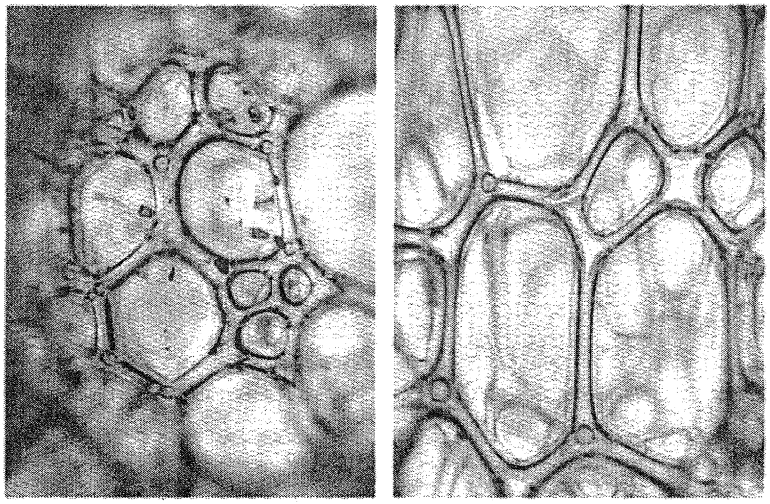

(a) (b)

Figure 1: Microphotographs of two cross sections in a low-density, open-cell polyurethane solid foam of measured apparent density $\rho_a = 51.6\,\mathrm{Kgm}^{-3}$ (General Plastics EF-4003). a) Section normal to the rise direction. b) Section parallel to the rise direction.

Polymeric solid foams are manufactured by heating sheets made of a polymer mixed with a foaming agent (Artavia & Macosko 1994). The foaming agent promotes the growth of numerous gas bubbles within the sheet, which expands anisotropically, mostly along a direction normal to its mid-plane—the so-called *rise direction*. Figure 1 shows the microstructure of a polyurethane foam of low relative density. (The relative density is defined as $\rho \equiv \rho_a/\rho_s$, where ρ_a is the apparent density of the foam, and ρ_s is the density of the solid part, in the case of figure 1 the polyurethane.) The plane of figure 1a is normal, whereas that of figure 1b is parallel to the rise direction. We can aptly describe the microstructure of figure 1 as a three-dimensional network of bars of similar length and cross section. The network appears to be composed of repeated groups of bars or *open cells*, which is why these foams are called open-cell foams. Depending on the polymer, the foaming agent, and the processing conditions, a *closed-cell* foam may obtain instead of an open-cell foam. The closed cells are in this case roughly ellipsoidal, thin shells. Because of the stiffening effect of the gas trapped in their cells, closed-cell foams behave rather differently than open-cell foams.

In this paper we study the deformation of open-cell, elastic solid foams. Figure 2 shows the mechanical response of the foam of figure 1 subject to uniaxial compressive stretch. The σ–λ curve of figure 2 is characteristic of compressed open-cell foams of low relative density; it is composed of a linear portion, a stress plateau, and a hardening portion. The most interesting feature of this σ–λ curve is the wide stress plateau.

The stress plateau of figure 2 is related to the buckling of the network of bars of figure 1. We have documented this buckling process in figure 3. Based on the calculation of buckling loads and post-buckling displacements, a buckling model has been used to predict with good

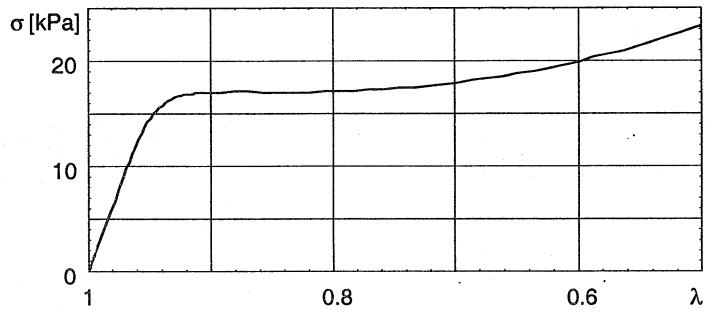

Figure 2: Mechanical response of the foam of figure 1 subject to uniaxial compressive stretch in the rise direction. A stretch $\lambda = 1$ corresponds to the undeformed geometry, whereas stretches $\lambda < 1$ correspond to compressed geometries.

results the width of the plateau and the associated value of stress.[1] Other aspects of the behavior of compressed solid foams have not been properly addressed, however. Thus, it is known that the stretch is spatially heterogeneous in a foam which has been compressed into the stress plateau (Shaw & Sata 1966; Vaz & Fortes 1993; the stretch heterogeneity has been beautifully—albeit only qualitatively—documented in brittle foams, see Kurauchi et al. 1984, and honeycombs, see Papka & Kyriakides 1994). This means that the buckling of figure 3 does not occur *simultaneously* everywhere in the foam. In spite of its strengths, the buckling model is not particularly illuminating of this deformation habit, at least in its present form.

In this paper we show that the stretch heterogeneity observed in experiments can be best elucidated by considering the energetics of solid-foam deformation. The advantage of focusing on the energetics may be readily grasped with the help of figure 4, which we have obtained using a simple model to be introduced in §2. Figure 4a pertains to a low-density open-cell foam; it represents the strain energy per unit volume of foam as a function of the applied uniaxial stretch, $\phi(\lambda)$. The key feature of this function is that it is nonconvex, that is to say, that $\phi''(\lambda) < 0$ over a portion $\lambda_1 > \lambda > \lambda_2$ of its domain. For high-density foams, on the other hand, $\phi(\lambda)$ is convex, e.g. figure 4b. Nonconvex energy functions are characteristic of numerous physical systems in which heterogeneous spatial fields are known to obtain in association with specific processes. Perhaps the most conspicuous instance is the van der Waals model of a gas of weakly interacting molecules. At sufficiently low temperatures, the isothermal liquefaction of van der Waals gases takes place in a range of *overall* (or average) specific volumes, wherein the gaseous and liquid phases coexist. Other instances of such processes include the solidification of certain alloys (Cahn 1961), the deformation of martensites (Khachaturyan 1983), the epitaxial growth of thin films (Orme & Orr 1997), the plastic deformation of crystals (Ortiz & Repetto 1999), and the magnetization of ferromagnets (James & Kinderlehrer 1990), where heterogeneous fields have

[1]For a review of the buckling model see Gibson & Ashby 1997. It is noteworthy that in this model the microstructure of the foam is assumed to buckle in the sense of Euler, i.e. involving a bifurcation of equilibrium. Instead, figure 3 seemingly suggests that the microstructure undergoes snap-through buckling, with no bifurcation of equilibrium, in the way envisioned in our model of §2.

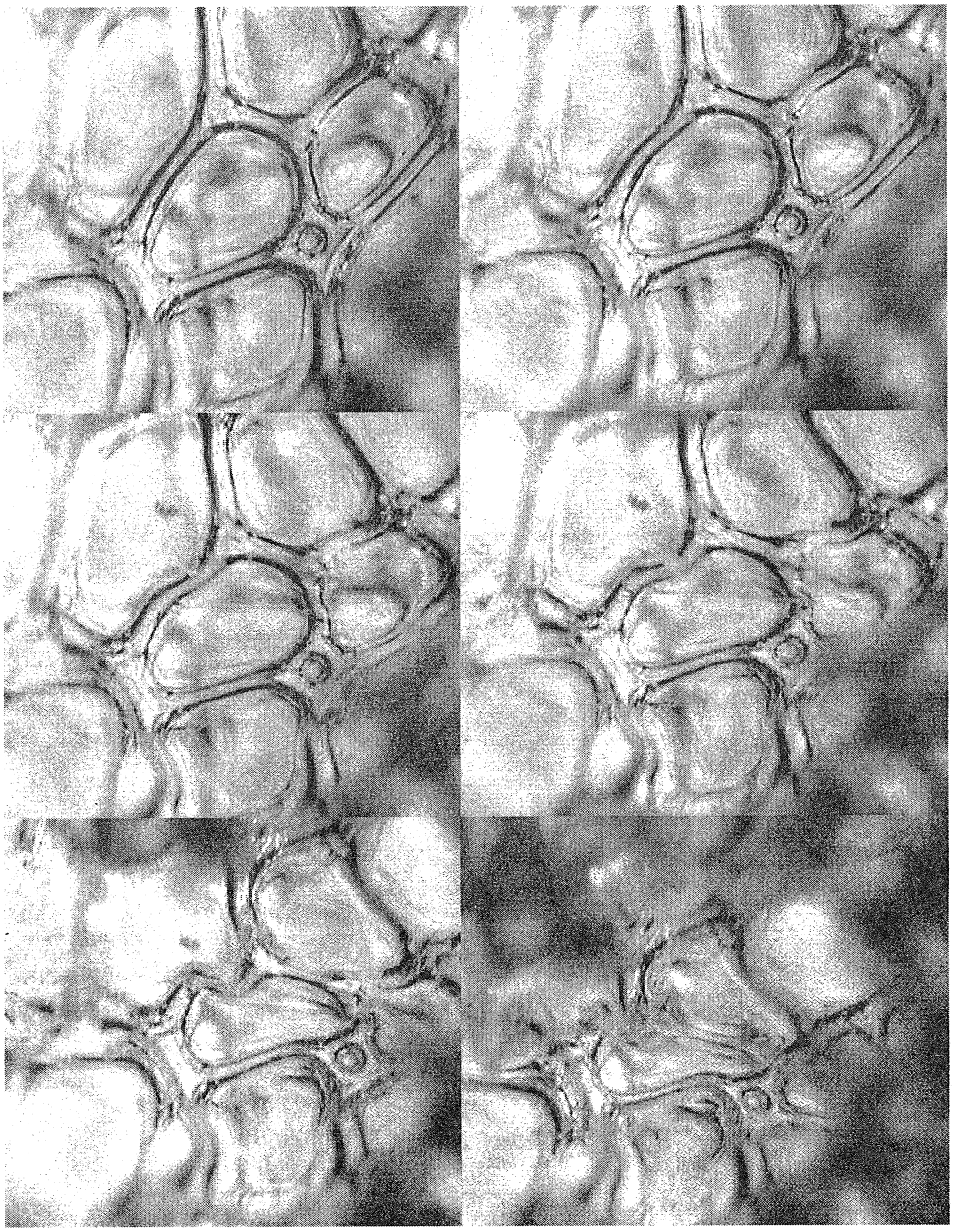

Figure 3: Buckling of the microstructure of figure 1. The sequence goes from left to right and top to bottom. The cells appear to be equiaxed (cf. figure 1b) because the line of view is not perpendicular to the rise direction.

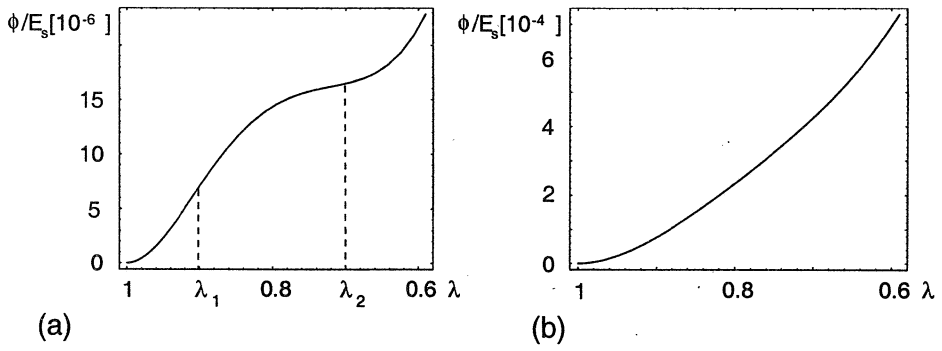

Figure 4: Internal energy density functions of uniaxially stretched open-cell solid foams. E_s is the Young's modulus of the solid part of the foam. a) Foam of relative density $\rho = 0.014$. b) Foam of relative density $\rho = 0.08$.

been documented in the form of eutectic structures, twinning, film roughening, dislocation cells, and magnetic domain structures, respectively. Further examples are afforded by the coagulation of gels (Carr & Pego 1992), the folding of compressed thin films (Gioia et al. 2000), the self-assembly of polymer layers on patterned substrates (Böltau et al. 1998), and the coarsening of froths (Aref & Vainchtein 2000).

In §4 we use energy methods to show that the heterogeneous stretch fields observed in compressed low-density foams correspond to mixtures of two *configurational phases* of the foam. These phases are defined by characteristic values of the local stretch. While the two phases coexist in a foam specimen, the specimen deforms at a constant stress (the plateau stress of figure 2), by the growth of the volume fraction of one of the phases at the expense of the volume fraction of the other phase; in other words, the deformation occurs in the form of a *phase transformation*. In §6 we compare experimental and predicted σ–λ curves for a series of foams of different densities. Finally, in §7 we measure full-field stretch distributions using the digital image correlation technique, and show that the obtained fields correspond to mixtures of two characteristic phases, as predicted by the theory.

2 Model

In this section we introduce a simple model for open-cell foams subject to uniaxial stretch. We start by representing the microstructure of figure 1 as a regular network of bars, figure 5a, composed of identical four-bar cells, figure 5b. If the foam is stretched uniaxially along the rise direction, and the bars of length L_1 do not buckle, we can model the four-bar cells of figure 5b in the form of two-bar structures, see figure 5c. The bars have a circular cross section of radius r and area $A = 4\pi r^2$. Thus the initial geometry of the network of bars is fully determined by three dimensionless parameters: $\tilde{r} \equiv r/L$, $\tilde{L}_1 \equiv \tilde{L}_1/L$, and the angle α. We assume the material of the bars (i.e. the solid part of the foam) to be linear elastic of Young's modulus E_s. The bars are ruled by Von Kármán's theory of beams. The equations

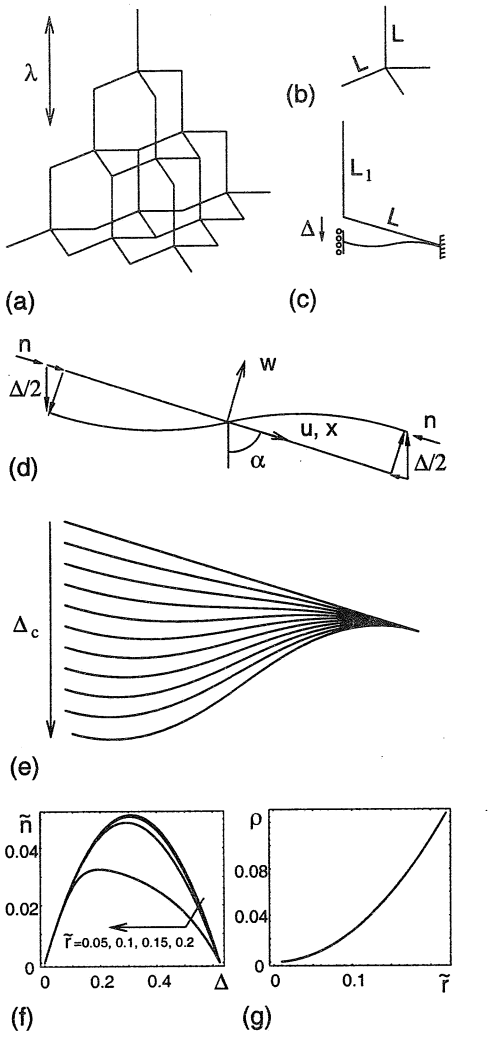

Figure 5: A simple model for open-cell solid foams stretched in the rise direction. a) The foam microstructure of figure 1 represented as a regular network of bars. The stretch is to be applied in the rise direction, as indicated. b) A component four-bar cell. c) Under the conditions discussed in the text, the four-bar cells simplify to two-bar structures, such as this one, where the bar of length L is in actuality three bars of equal cross section. d) Analysis of the bar of length L; $n > 0$ is the compressive axial force. The following are examples for $\tilde{L}_1 = 2.5$ and $\alpha = \cos^{-1}(1/3)$: e) Deflection functions $\tilde{w}(\tilde{x})$ for eleven equidistant values of the dimensionless displacement $\tilde{\Delta}$ in the range $0 < \tilde{\Delta} < \tilde{\Delta}_c$. f) The dimensionless compressive axial force $\tilde{n}$ as a function of $\tilde{\Delta}$ for four different values of the dimensionless cross-sectional radius $\tilde{r}$. g) Relative density of the foam as a function of $\tilde{r}$.

of equilibrium for any one of the bars of length L are:

$$\tilde{r}^2\tilde{w}''''/4 + (\tilde{n}\tilde{w}')' = 0 \tag{1}$$

and

$$\tilde{n}' = 0, \tag{2}$$

where

$$\tilde{n} \equiv n/E_s A = -(\tilde{u}' + \tilde{w}'^2/2), \tag{3}$$

$\tilde{w} \equiv w/L$, $\tilde{u} \equiv u/L$, $\tilde{x} \equiv x/L$, see figure 5d, and $(\cdot)' \equiv d(\cdot)/d\tilde{x}$. From (2) we have $\tilde{n} = \text{const.}$; then (1) along with the boundary conditions $\tilde{w}(\pm 1/2) = \pm\tilde{\Delta}\sin(\alpha)/2$ and $\tilde{w}'(\pm 1/2) = 0$ (where $\tilde{\Delta} \equiv \Delta/L$) leads to

$$\tilde{w} = \tilde{\Delta}\sin(\alpha)\frac{\tilde{x}\sqrt{\tilde{n}}\cos\left(\sqrt{\tilde{n}}/\tilde{r}\right) - \tilde{r}\sin\left(2\tilde{x}\sqrt{\tilde{n}}/\tilde{r}\right)/2}{\sqrt{\tilde{n}}\cos\left(\sqrt{\tilde{n}}/\tilde{r}\right) - \tilde{r}\sin\left(2\tilde{x}\sqrt{\tilde{n}}/\tilde{r}\right)}. \tag{4}$$

We can now use (3) to obtain an expression for $\tilde{u}$, which expression leads upon imposition of the boundary conditions $\tilde{u}(\pm 1/2) = \mp\tilde{\Delta}\cos(\alpha)/2$, figure 5d, to an implicit nonlinear equation for the eigenvalue $\tilde{n}$:

$$\begin{aligned} &4\left(\tilde{n} - \tilde{\Delta}\cos(\alpha)\right)\left(\sqrt{\tilde{n}}\cos(\sqrt{\tilde{n}}/\tilde{r}) - r\sin(\sqrt{\tilde{n}}/\tilde{r}\right)^2 + \\ &\sqrt{\tilde{n}}\,\tilde{\Delta}^2\left(\sqrt{\tilde{n}}\left(2 + \cos(2\sqrt{\tilde{n}}/\tilde{r})\right) - 3\tilde{r}\sin(2\sqrt{\tilde{n}}/\tilde{r})/2\right)\sin(\alpha)^2 = 0. \end{aligned} \tag{5}$$

From (5) we conclude, firstly, that $\tilde{n}$ cannot be expressed as a function of a single parameter involving both $\tilde{\Delta}$ and $\tilde{r}$; and, secondly, that $\tilde{n}$ vanishes, regardless of the value of $\tilde{r}$, when $\tilde{\Delta} = 0$, but also when $\tilde{\Delta} \to \tilde{\Delta}_c \equiv 5\cot(\alpha)\csc(\alpha)/3$. Equations (4) and (5) allow for the computation of deflection curves $\tilde{w}(\tilde{x})$, e.g. figure 5e. Figure 5f shows example plots of $\tilde{n}(\tilde{\Delta})$ for a series of values of $\tilde{r}$.

The strain energy of the three bars of length L is given by

$$\frac{W_L}{E_s A L} = \frac{3}{2}\int_{-1/2}^{1/2}\left(\tilde{r}^2(\tilde{w}'')^2/4 + \tilde{n}^2\right)d\tilde{x}. \tag{6}$$

The strain energy of the bar of length L_1 is

$$\frac{W_{L_1}}{E_s A L} = \frac{9}{2}\tilde{n}^2\tilde{L}_1\cos^2(\alpha). \tag{7}$$

We can now write an expression for the strain energy density of the foam by dividing the strain energy of one cell (i.e. of three bars of length L plus one bar of length L_1) into the tributary volume of the cell (in the original geometry); the result is

$$\begin{aligned} \frac{\phi}{E_s} &= \frac{4\pi\tilde{r}^2}{3\sqrt{3}\sin^2(\alpha)\left(\tilde{L}_1 + \cos(\alpha)\right)} \times \\ &\left(\frac{3\tilde{\Delta}^2\tilde{n}^{3/2}\sin^2(\alpha)\left(\sqrt{\tilde{n}} - \tilde{r}\sin(2\sqrt{\tilde{n}}/\tilde{r})\right)}{4\left(\sqrt{\tilde{n}}\cos(\sqrt{\tilde{n}}/\tilde{r}) - \tilde{r}\sin(2\sqrt{\tilde{n}}/\tilde{r})\right)} + \frac{3\tilde{n}^2}{2} + \frac{9}{2}\tilde{n}^2\tilde{L}_1\cos^2(\alpha)\right). \end{aligned} \tag{8}$$

In the order of their appearance, the three terms in the large parenthesis on the right hand side of (8) represent the bending energy of the bars of length L, the axial energy of the bars of length L, and the axial energy of the bar of length L_1. We verify that the energy density ϕ vanishes for $\tilde{\Delta} = 0$. When $\tilde{\Delta} = \tilde{\Delta}_c$, on the other hand, $\phi = 50\, E_s\, \tilde{r}^2 \cot^2(\alpha)/3$, which is pure bending energy.

Finally, straightforward geometry leads to the following expressions for the stretch,

$$\lambda = 1 - \frac{1}{\tilde{L}_1/2 + \cos(\alpha)} \left(\tilde{\Delta} + 3\tilde{n}\tilde{L}_1 \cos(\alpha)/2 \right), \tag{9}$$

and for the relative density in the original geometry,

$$\rho = \frac{2\pi\tilde{r}^2 \left(3 + \tilde{L}_1^2\right) \csc^2(\alpha)}{3\sqrt{3} \left(\tilde{L}_1 + \cos(\alpha)\right)}. \tag{10}$$

For a set of values of α, $\tilde{L}_1$, and $\tilde{r}$ (i.e. a foam microstructure), (10) gives the relative density; the associated strain energy density function follows parametrically from (8) and (9) by allowing the dimensionless displacement $\tilde{\Delta}$ to span the admissible range $0 \leq \tilde{\Delta} \leq \tilde{\Delta}_c$. We have seen examples of $\phi(\lambda)$ functions in figure 4; in the following sections we study the energetics of solid foams governed by strain energy density functions such as those of figure 4. We base our exposition on Pipkin (1993).

3 Energy minimization

We study a foam specimen of height H (denoted in italics) and unit cross-sectional area. The specimen is compressed to an overall stretch $\bar{\lambda}$. Consider the function $x(X)$ which maps the original geometry X into the current geometry x, figure 6a-b, where $x(0) = 0$ and $x(H) = \bar{\lambda}H$. The local values of stretch and stress are $\lambda(X) = x'(X)$ and $\sigma(X) = -\phi'(\lambda(X))$, respectively ($\sigma > 0$ is compressive). Under these conditions, the height of the specimen in the current geometry is fixed, and the applied forces do not perform work. Then, the total potential energy functional of the specimen is

$$\Phi\left[x(X)\right] = \int_0^H \phi(x'(X))\, dX. \tag{11}$$

We are interested in finding the mapping $x(X)$ which effects the minimization of Φ.

We start by introducing a perturbed mapping $x(X) + \epsilon\, v(X)$, where ϵ is a scalar parameter and $v(X)$ is an admissible variation subject to the essential boundary conditions $v(0) = v(H) = 0$. We substitute the perturbed mapping into (11), and expand the resulting expression $\Phi(\epsilon)$ in Taylor series around $\epsilon = 0$, up to the second order in ϵ, to obtain

$$\Phi(\epsilon) = \int_0^H \phi(x'(X))\, dX + \epsilon \int_0^H \phi'(x'(X))\, v'(X)\, dX + \frac{\epsilon^2}{2} \int_0^H \phi''(x'(X)) v'(X)^2 dX + o(\epsilon^3). \tag{12}$$

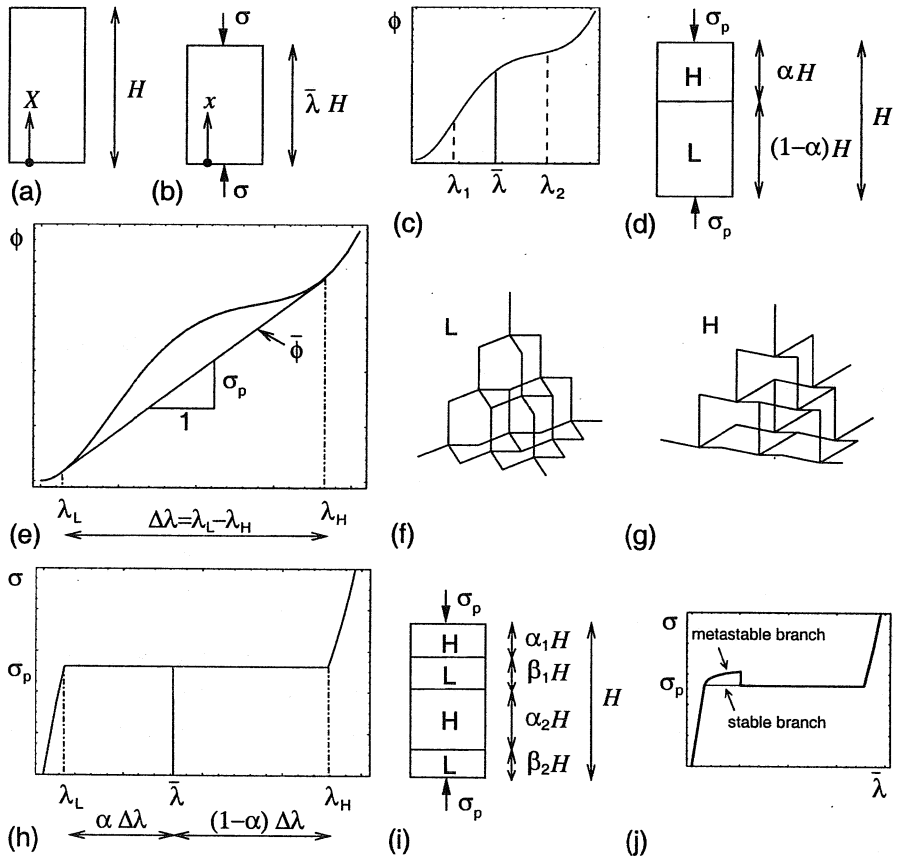

Figure 6: Energy analysis of a specimen of low-density foam. a) Original geometry. b) Current geometry. $\bar{\lambda}$ is the applied overall stretch. c) Nonconvex strain energy function $\phi(\lambda)$; $\phi''(\lambda_1) = \phi''(\lambda_2) = 0$. d) A family of heterogeneous stretch distributions. e) Graphical interpretation of the Erdmann equilibrium equations (19). f) The low-density phase L (schematic). g) The high-density phase H. h) Stress vs. overall stretch. Note the stress plateau associated with the phase transformation L→H. i) Example of stratified mixture of the L and H phases. $\alpha_1 + \alpha_2 + \beta_1 + \beta_2 = 1$. j) A limited excursion along the metastable branch.

In performing the Taylor expansion (12) we are confining the perturbed mapping and its derivative to limited vicinities of $x(X)$ and $x'(X)$; this means that any minimizing mapping picked up by (12) may correspond to a *local* minimum of Φ, not necessarily a global minimum. For $x(X)$ to make Φ stationary we require $\Phi'(\epsilon)|_{\epsilon=0} = 0$, i.e.

$$\int_0^H \sigma(X)\, v'(X)\, dX = 0, \tag{13}$$

where we have used $\sigma(X) = -\phi'(x'(X))$. After integrating by parts, (13) results in the Euler-Lagrange extremum or *equilibrium* equation, $\sigma'(X) \equiv 0$. Thus equilibrium requires a spatially homogeneous distribution of stress.

A spatially homogeneous stretch distribution always satisfies the equilibrium equation; to test whether it minimizes Φ, we substitute $x'(X) \equiv \bar{\lambda}$ into (12), and impose $\Phi''(\epsilon)|_{\epsilon=0} \geq 0$, i.e.

$$\int_0^H \phi''(\bar{\lambda}) v'(X)^2 dX \geq 0, \tag{14}$$

which should hold for all admissible variations $v(X)$. The Legendre-Hadamart *stability* condition follows immediately in the form

$$\phi''(\bar{\lambda}) \geq 0. \tag{15}$$

When $\phi(\lambda)$ is convex, the Legendre-Hadamart stability condition is readily fulfilled for any given value of $\bar{\lambda}$. That is the case for foams of large relative densities, figure 4b. For these foams we expect the stretch to be spatially homogeneous for any value of applied overall uniaxial stretch; as $\bar{\lambda}$ decreases during stretching, the stress should increase monotonically, with no stress plateau. This is, in fact, the observed behavior of large-density foams. On the other hand, for foams of low relative densities the stability condition is violated when $\lambda_1 > \bar{\lambda} > \lambda_2$, figure 4a. We study the implications of this fact in the following section.

4 Two-phase stretching modes

We consider once more the specimen of figure 6a-b, made of a low density foam of nonconvex strain energy density function $\phi(\lambda)$, and subject to an overall stretch $\bar{\lambda}$. If $\lambda_1 > \bar{\lambda} > \lambda_2$, figure 6c, a homogeneous stretch distribution $\lambda(X) \equiv \bar{\lambda}$ of total energy $\Phi_h = \phi(\bar{\lambda})H$ violates the Legendre-Hadamart stability condition (15), and cannot be realized. It is possible to show, however, that for any given applied overall stretch in the range $\lambda_1 > \bar{\lambda} > \lambda_2$, *infinitely many heterogeneous stretch distributions exist which are both equilibrated and stable, and therefore solutions.*

We start by finding one family of such heterogeneous stretch distributions. (There is one member of the family for each value of $\bar{\lambda}$. We leave the issue of the existence of other families, i.e. the lack of uniqueness, for §5.) To that end we split the height H of the specimen into one region of height αH, to which we assign a uniform local stretch $\lambda_H < \bar{\lambda}$,

and a second region of height $(1-\alpha)H$, to which we assign a uniform local stretch $\lambda_{\rm L} > \bar{\lambda}$, figure 6d. (The subscripts L and H—in Roman type—stand for low and high *current value* of density, respectively.) For the overall stretch to remain equal to $\bar{\lambda}$ we must satisfy the *rule of mixtures*

$$\alpha = \frac{\lambda_{\rm L} - \bar{\lambda}}{\lambda_{\rm L} - \lambda_{\rm H}}. \tag{16}$$

The average energy density of the specimen is then a function of $\lambda_{\rm L}$ and $\lambda_{\rm H}$,

$$\phi^*(\lambda_{\rm L}, \lambda_{\rm H}) = \alpha\phi(\lambda_{\rm H}) + (1-\alpha)\phi(\lambda_{\rm L}). \tag{17}$$

We impose equilibrium by making $\phi^*(\lambda_{\rm L}, \lambda_{\rm H})$ stationary subject to the subsidiary condition (16). This we effect by finding the stationary point $(\lambda_{\rm L},\ \lambda_{\rm H},\ \sigma_p)$ of the auxiliary function

$$\phi^{**}(\lambda_{\rm L}, \lambda_{\rm H}, \sigma_p) \equiv \phi^*(\lambda_{\rm L}, \lambda_{\rm H}) - \sigma_p\left(\alpha\lambda_{\rm H} + (1-\alpha)\lambda_{\rm L} - \bar{\lambda}\right), \tag{18}$$

where σ_p is a Lagrange multiplier. We call the solving values of $\lambda_{\rm L}$, $\lambda_{\rm H}$, and σ_p the *characteristic stretches* and the *plateau stress*, respectively; they are given by the Erdmann equilibrium equations:

$$\sigma_p = -\frac{\Delta\phi}{\Delta\lambda} = -\left.\phi'(\lambda)\right|_{\lambda=\lambda_{\rm L}} = -\left.\phi'(\lambda)\right|_{\lambda=\lambda_{\rm H}}, \tag{19}$$

where $\Delta\phi \equiv \phi(\lambda_{\rm L}) - \phi(\lambda_{\rm H})$, and $\Delta\lambda \equiv \lambda_{\rm L} - \lambda_{\rm H}$, see figure 6e. It bears emphasis that the solving values $\lambda_{\rm L}$, $\lambda_{\rm H}$, and σ_p given by (19) depend exclusively on the strain energy density function, $\phi(\lambda)$, and may be construed as material properties. The characteristic stretches $\lambda_{\rm L}$ and $\lambda_{\rm H}$ correspond to two different configurational phases of the microstructure: a low-density phase L and a high-density phase H, which obtain before and after snap-through buckling, respectively, see figures 6f-g, 5e, and 3. We conclude that the two-phase stretch distributions of figure 6d, with $\lambda_{\rm L}$ and $\lambda_{\rm H}$ given by (19), are equilibrated under a spatially homogeneous stress $\sigma(X) \equiv \sigma_p$, where σ_p is also given by (19). One such two-phase stretch distribution exists for each value of applied overall stretch in the range $\lambda_{\rm L} > \bar{\lambda} > \lambda_{\rm H}$. When $\bar{\lambda}$ decreases during stretching from $\lambda_{\rm L}$ to $\lambda_{\rm H}$, the volume fraction α increases from 0 to 1, and the stress remains constant and equal to the plateau stress, figure 6h, just as it is observed in experiments on low-density foams, figure 2. Thus stretching occurs by growth of the high-density phase H at the expense of the low-density phase L, in the form of a phase transformation L→H. As the phase transformation proceeds, each member of the family of stretch distributions of figure 6d is visited in turn. The average energy density attendant to two-phase stretch distributions is given by the convexified form

$$\begin{aligned} \bar{\phi}(\lambda) &\equiv \alpha(\lambda)\phi(\lambda_{\rm H}) + (1-\alpha(\lambda))\phi(\lambda_{\rm L}), \\ \alpha(\lambda) &= (\lambda_{\rm L} - \lambda)/(\lambda_{\rm L} - \lambda_{\rm H}), \end{aligned} \tag{20}$$

which within the range $\lambda_{\rm L} > \bar{\lambda} > \lambda_{\rm H}$ yields the correct value $\sigma = -\left.\bar{\phi}'(\lambda)\right|_{\lambda=\bar{\lambda}} = \sigma_p$, figure 6e. It is apparent that $\bar{\phi}(\lambda) \leq \phi(\lambda)$ for all λ.

We now ascertain the stability of the two-phase stretch distributions of figure 6d. Consider an *arbitrary* comparison distribution $\lambda_c(X) = x_c'(X)$ with $x_c(0) = 0$, $x_c(H) = \bar{\lambda}H$,

and $\lambda_{\mathrm{L}} \leq \lambda_c(X) \leq \lambda_{\mathrm{H}}$ for all X. The energy functional evaluated at $x_c(X)$ is

$$\Phi\left[x_c(X)\right] = \int_0^H \phi(x_c'(X))\, dX \geq \int_0^H \bar{\phi}(x_c'(X))\, dX. \tag{21}$$

We now introduce the two-phase stretch distribution $\lambda(X) = x'(X)$ corresponding to the given value of $\bar{\lambda}$. Then, on account of the fact that $\bar{\phi}'(x'(X)) = -\sigma_p$ for all X, the following expression is fulfilled for all X,

$$\bar{\phi}\left(x_c'(X)\right) = \bar{\phi}(x'(X)) - \sigma_p \left(x_c'(X) - x'(X)\right). \tag{22}$$

Integrating both sides of (22) from $X = 0$ to $X = H$ we obtain

$$\int_0^H \bar{\phi}(x_c'(X))\, dX = \Phi\left[x(X)\right], \tag{23}$$

where we have used $\Phi\left[x(X)\right] = \int_0^H \bar{\phi}(x'(X))\, dX$ and the boundary conditions $x(0) = x_c(0) = 0$ and $x(H) = x_c(H) = \bar{\lambda}H$. From (21) and (23) it follows that

$$\Phi\left[x(X)\right] \leq \Phi\left[x_c(X)\right]. \tag{24}$$

Thus the energy functional attains a *global* minimum at the two-phase stretch distribution $\lambda(X) = x'(X)$. An interesting choice of comparison distribution is $\lambda_c(X) \equiv \bar{\lambda}$, with $\bar{\lambda}$ in either of the intervals $\lambda_{\mathrm{L}} < \bar{\lambda} < \lambda_1$ or $\lambda_2 < \bar{\lambda} < \lambda_{\mathrm{H}}$. Even though this $\lambda_c(X)$ is a stable stretch distribution (because it fulfills the Legendre-Hadamart stability condition), (24) shows that the energy attendant to $\lambda_c(X)$ is larger than the energy attendant to the corresponding two-phase distribution. This means that the energy attains a *local* minimum at the homogeneous distribution $\lambda_c(X) \equiv \bar{\lambda}$, or, equivalently, that $\lambda_c(X)$ corresponds to a *metastable* state (Ericksen 1998). Metastable states are sometimes realized in practice; in fact, in uniaxial stretching tests it is a common occurrence for the foam to follow the metastable branch after passing the point $\bar{\lambda} = \lambda_{\mathrm{L}}$. Eventually, the foam switches to a two-phase stretch distribution, in the form sketched in figure 6k. This sort of behavior has been pointed out by other authors, but does not seem discernible in figure 2.

5 Lack of uniqueness

It is apparent that besides the stretch distribution of figure 6d, any other *stratified* mixture of the two characteristic phases, in the volume fractions appropriate to the applied $\bar{\lambda}$, is also equilibrated under a constant stress σ_p. For any given value of $\bar{\lambda}$, infinitely many such stratified stretch distributions exist, e.g. figure 6i; it is easy to verify that all of them correspond to the same global minimum of the energy functional. (The equal sign in (24) applies when both $\lambda(X)$ and $\lambda_c(X)$ are two-phase distributions.) It follows that the spatial distribution of phases is not fully determined by our analysis. This lack of uniqueness is endemic in problems involving nonconvex energy functionals. A solution which originated with the pioneering work of de Giorgi (1975) is to resort to higher-order terms of the

energy functional for selecting a *preferred* stretch distribution. In the present context, the foam possesses a microstructure endowed with a scale length, figure 5, which precludes the realization of a sharp stretch jump $[\![\lambda]\!] = \lambda_{\mathrm{L}} - \lambda_{\mathrm{H}}$ across the H-L interfaces. This means that, in actuality, the stretch jump spreads over layers of finite width centered at the H-L interfaces. In principle, we could perform a boundary layer analysis to accord a well-defined energy per unit area to the H-L interfaces (Modica 1987; Kohn & Müller 1994). The preferred stratified stretch distribution would then follow from minimizing the *number* of H-L interfaces (Gioia & Ortiz 1997). This conclusion would bring us back to the family of distributions of figure 6d, whose members contain a single H-L interface. In practice, which stretch distribution will obtain in a given specimen depends on local irregularities in the microstructure of the foam, where nuclei of H are likely to form. In fact, distributions with several H-L interfaces are not uncommon in experiments (see §7). When the energy attendant to the H-L interfaces is taken into account, these distributions are, strictly speaking, metastable.

6 Mechanical response: experiments and predictions

In figure 7 we compare the predictions of the model of §2, properly convexified, with experimentally obtained σ–$\bar{\lambda}$ and $\bar{\phi}$–$\bar{\lambda}$ curves for a series of foams of different densities. Even though we formulated the model to illustrate only the most salient features of the micromechanics of solid foams, and made no special effort to fit the experimental curves, the model gives a good description of the experiments. It is noteworthy that each of the predicted σ–$\bar{\lambda}$ curves stems from a single, smooth strain energy density function.

In §1 we pointed out that the stretching of low-density solid foams is analogous to the low-temperature, isothermal liquefaction of van der Waals gases. The analogy is made apparent by figure 7a, which bears a strong resemblance to the so-called *state diagrams* of van der Waals gases (as well as of many real substances). Thus the stress, stretch, and density of foams are formally analogous to the pressure, specific volume, and temperature of van der Waals gases, respectively. Just as is the case in state diagrams, the region of coexistence of two phases is bounded in figure 7a by an arch-shaped curve. The topmost point of this curve is the *critical point*, denoted by a letter C in figure 7a. We call *critical density* the density of the foam whose σ–$\bar{\lambda}$ curve contains the critical point; in the instance of figure 7a the critical relative density is $\rho_c = 0.056$. If it were feasible, at a constant applied overall stretch, to reduce the density of a foam from a value higher that ρ_c to a value lower that ρ_c, we would say that, in so doing, the foam undergoes a *second order transition* (Ericksen 1998).

The predicted σ–$\bar{\lambda}$ curves of figure 7a are based on convexified strain energy density functions. The good agreement with experiments, in particular in the range of sub-critical densities, where metastable states are possible (figure 6j), seems to indicate that for the most part the mechanical response of solid foams is governed by the global minimization of the total potential energy Φ, equation (11). This inference is not universally valid, however.

In §7 we shall find clear signs of a metastable excursion in the mechanical response of a foam of very low density. A similar behavior has been reported by Shaw & Sata (1966) and Vaz & Fortes (1993).

7 Experimental observation of stretch distributions

In this section we report the results of whole-field displacement measurements performed on the surface of a stretched foam using the Digital Image Correlation (DIC) technique. (On DIC see e.g. Peters & Ranson 1982; Kahn-Jetter & Chu 1990; and Vendroux & Knauss 1998. For an example of application to solid foams see Zhang et al. 1999.)

In our experiments we used a specimen made of a very light open-cell solid foam, to which we applied a uniaxial stretch. Figure 8 shows the mechanical response of the foam. We took 21 pictures of one of the lateral faces of the specimen, at equal intervals of $\bar{\lambda}$, and correlated the successive pictures, one pair at a time, to compute the displacement at the pixels of the reference images. Our aim was to detect *localized* deformation; consequently, we used a small correlation window, namely an array of 15×15 neighboring pixels, to provide displacement measurements with a standard deviation of 0.1 pixel. This is a compromise between spatial resolution and displacement accuracy. We transfered the cumulative displacement of each reference image to the successive reference image using a bilinear interpolation.

Figure 9a is a contour plot of the displacement field $u_X(X,Y)$ on a portion of the face of the specimen. (In the notation of figures 6a–b, $u_X(X,Y) = X - x(X,Y)$.) The overall stretch was $\bar{\lambda} = 0.74$ (picture 11). The heterogeneous nature of the stretch distribution is apparent in figure 9a. The zones of high and low local stretch form roughly parallel strata normal to the X direction, thus justifying our adoption of one-dimensional fields in the analysis of §3. To further scrutinize the displacement field of figure 9a we now turn to figure 9b, which shows a plot of the displacement u_X along the dotted line of figure 9a, i.e. $u_X(X, Y = 196)$. Two well-defined slopes $\partial u_X/\partial X$ are clearly discernible in figure 9b; they represent the low- and high-density phases. Indeed, it is easy to verify that the slope is related to the local stretch by the following expression:

$$\frac{\partial u_X}{\partial X} = \lambda - 1. \tag{25}$$

Figure 9b shows that the measured slopes compare well with the values computed with equation (25) using the characteristic values $\lambda = \lambda_{\mathrm{L}} = 0.91$ and $\lambda = \lambda_{\mathrm{H}} = 0.60$ obtained from figure 8. From figure 9b we can also estimate a volume fraction $\alpha = 0.33$; then, the rule of mixtures (16) leads to $\bar{\lambda} = 0.76$, which is in very good agreement with the experimental value $\bar{\lambda} = 0.74$. We conclude that the displacement field of figure 9a corresponds to one of the stratified two-phase stretch distributions discussed in §5.

Figure 10 shows plots of $u_X(X, Y = 196)$ for a series of values of applied overall stretch (pictures 1 to 21). For the first three values of $\bar{\lambda}$ the stretch distribution is homogeneous. Then, for the fourth value of $\bar{\lambda}$, the stretch is $\lambda(X) \sim \lambda_{\mathrm{L}} = 0.91$ over most of the domain

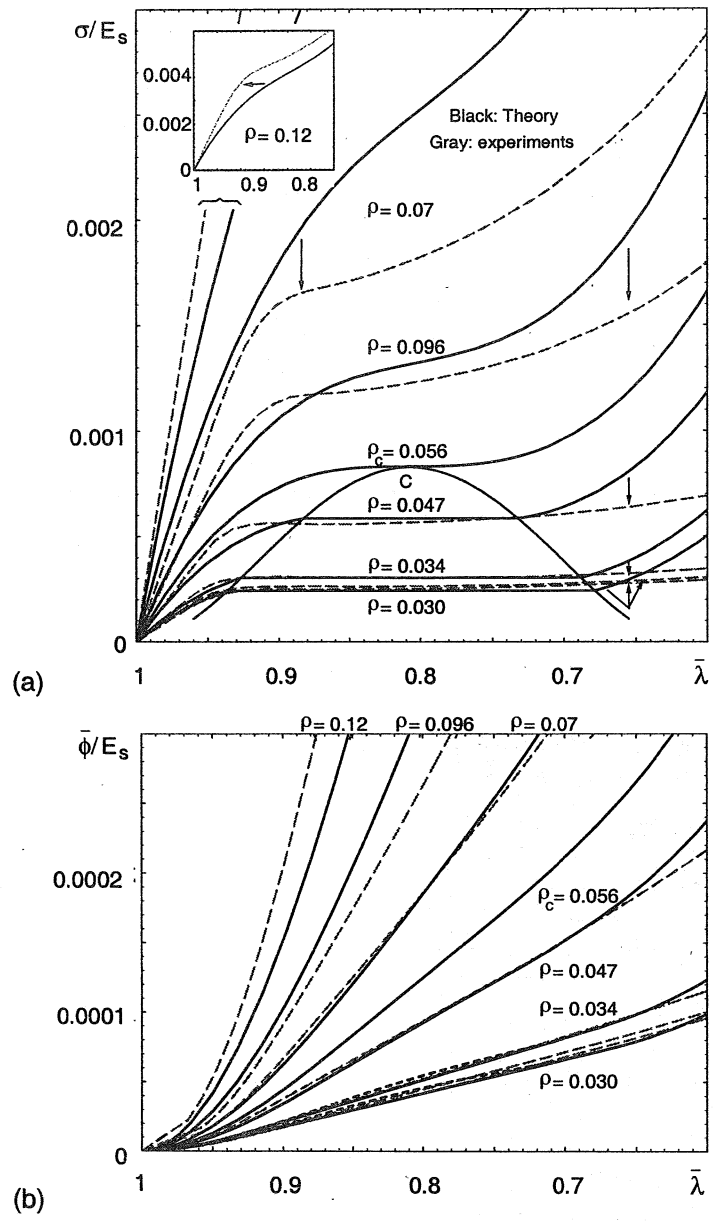

Figure 7: a) Experimental σ–$\bar{\lambda}$ curves (dashed gray lines) for six polyether polyurethane foams of measured apparent densities ρ_a = 51.6, 57.7, 80.2, 159, 219, and 280 Kgm^{-3} (General Plastics EF-4003, EF4004, EF4005, TF5070–10, TF5070–13, and TF5070–17, respectively). For the foam of the lowest density we show two $\sigma - \bar{\lambda}$ curves obtained using different specimens. To normalize the experimental curves we have used E_s = 65 MPa and ρ_s = 1,700 Kgm^{-3} (for the EF series) and ρ_s = 2,200 Kgm^{-3} (for the TF series); the resulting values of relative density ρ are indicated in the figure. The specimens had a cross section of 10.2 × 10.2 cm^2, and a height of 5.08 cm aligned with the rise direction. We repeatedly compressed the specimens in the rise direction, up to $\bar{\lambda} \sim 0.4$, and then unloaded; the obtained σ–$\bar{\lambda}$ curves were identical after three cycles. The curves shown are those for the fourth cycle. The speed of the loading plate was $4.2\,10^{-2}$ $\mathrm{cm\,s}^{-1}$. The predicted curves (black lines) are given by the model of section 2, properly convexified, with $L_1/L = 2.5$ and $\alpha = \cos^{-1}(1/3)$, see figures 5 and 1. b) Average strain energy density curves: experimental (dashed gray lines), obtained by numerical integration of the measured σ–$\bar{\lambda}$ curves; and predicted (black lines). The dashed black lines are the nonconvex portions of the predicted curves.

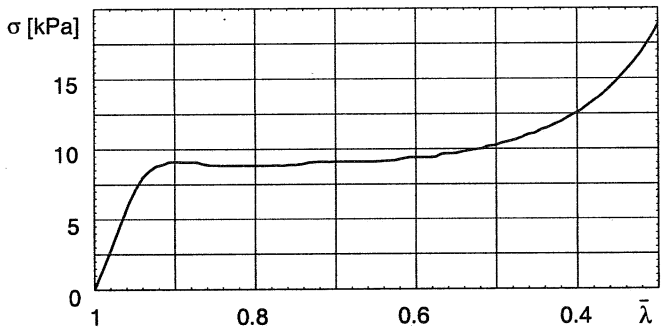

Figure 8: Mechanical response of the polyurethane foam used in the DIC experiments. The measured apparent density was $\rho_a = 24\,\mathrm{Kgm}^{-3}$. From this plot we obtain the following approximate values for the characteristic stretches: $\lambda_\mathrm{L} = 0.91$ and $\lambda_\mathrm{H} = 0.60$. The stress drop observed at $\lambda \sim 0.87$ marks the final stage of a brief metastable excursion.

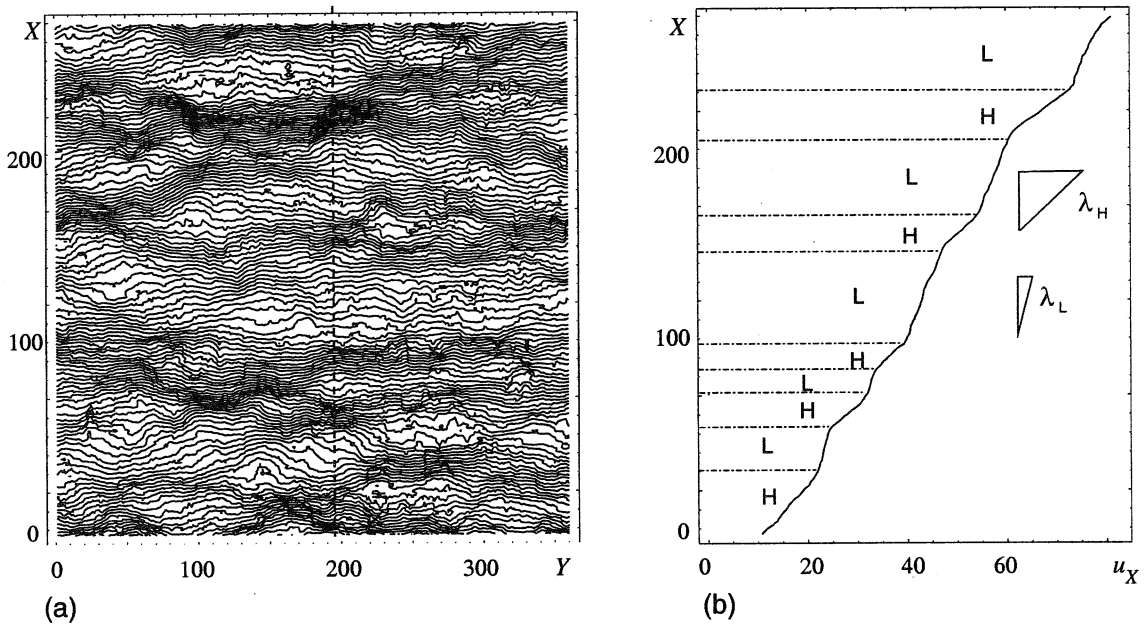

Figure 9: Displacement field measured by the DIC technique. The specimen had a cross section of $10.5 \times 3.72\,\mathrm{cm}^2$, and a height of 2.54 cm aligned with the rise direction (the X axis). We compressed the specimen in the rise direction. a) Contour plot of the displacement field $u_X(X, Y)$ on the surface of the specimen for $\bar{\lambda} = 0.74$. u_X is the displacement in the rise direction, and X is measured in the original geometry. The units of X, Y, and u_X are pixels. The plot consists of lines of equal u_X at regular intervals Δu_X. b) Plot of the displacement u_X along the dotted line of (a). The indicated slopes correspond to $\lambda_\mathrm{L} = 0.91$ and $\lambda_\mathrm{H} = 0.60$ (from figure 8).

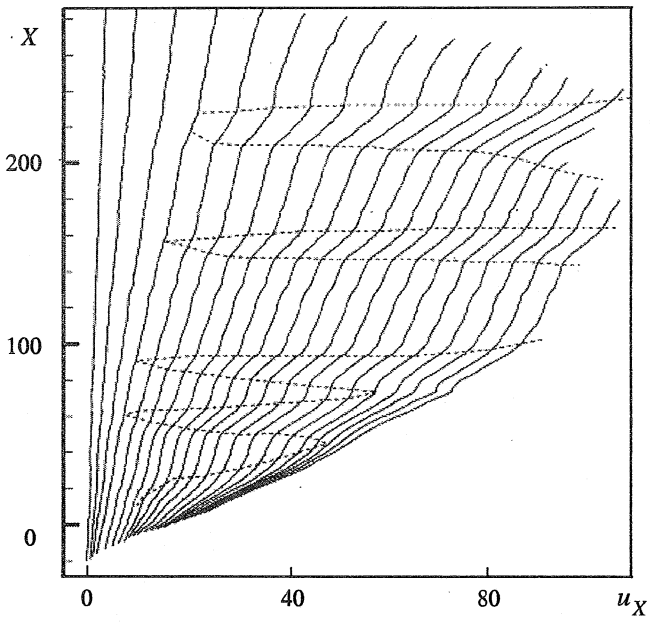

Figure 10: Plot of the displacement u_X along the dotted line of figure 9a for a series of values of applied overall stretch. The plot documents the process of nucleation and growth of five strata of the high-density phase H.

of X, with the exception of four narrow intervals wherein $\lambda(X) < \lambda_{\mathrm{L}}$. We construe these narrow intervals as nuclei of the high-density phase H. Our interpretation is confirmed by the subsequent growth of the intervals of lower local stretch into fully developed strata of H. As $\bar{\lambda}$ continues to decrease, the strata of H become thicker: figure 8 shows that this process takes place in coincidence with the stress plateau. Eventually, a fifth nucleus obtains at $X \sim 20$, which in turn grows into a high-density-phase stratum.

As discussed in §5, nucleation of the high-density phase is likely to occur at local points of irregularity in the microstructure of the foam. A very irregular microstructure may lead to the establishment of highly stratified two-phase stretch distributions, with a large number of H-L interfaces. Figure 10 shows that the slope $\partial u_X/\partial X$ changes smoothly across the H-L interfaces;[2] this is due to the presence of interface layers, which layers endow the H-L interfaces with a surface energy. By virtue of the surface energy associated with the H-L interfaces, highly stratified two-phase stretch distributions correspond, strictly speaking, to metastable states (cf. §5). We conclude that during the nucleation process irregular foams tend to become locked in states of high H-L interface energy. The results of Shaw

[2]A possible exception is afforded by the interface at $X \sim 210$, which appears to be quite sharp, at least for relatively small values of $\bar{\lambda}$. Shaw & Sata (1966) have argued that sharp H-L interfaces, devoid of surface energy, could be realized by the high-density strata becoming tilted by a small angle with respect to the Y-direction. This tilting appears to have happened in their experiments, but we discern no clear evidence of systematic tilting in Figure 9a.

& Stata (1966) and Vaz & Fortes (1993), in which at most two H-L interfaces appear to have been present, suggest that the foams used by those authors possessed more regular microstructures than the foam employed in our experiment.

8 Discussion

Our model of §2 is based on the behavior of a single, generic cell which snap-through buckles between the characteristic configurations of figures 6f–g. For a single cell it would be meaningless to speak of those configurations as phases, however: if we could control the displacement Δ_i of one arbitrary cell i, and increased Δ_i from 0 to Δ_c, the cell would in turn adopt each of the configurations shown in figure 5e, including the characteristic configurations, but the latter would play no special role in the process. This conclusion serves to stress a key element of our model, namely *homogenization*, by which we mean the expression of the mechanical behavior of a generic cell in terms of the strain energy density and stretch of an *equivalent continuum*. Any given portion of the equivalent continuum stands for very many identical cells of the microstructure of the foam.[3] As a result, when the equivalent continuum is subject to an overall stretch, only the sum $\Sigma\Delta_i$ over the underlying cells is fixed, but not the individual values Δ_i themselves, which are in principle free to accommodate the total displacement in a number of ways. It is on this freedom inherent to the equivalent continuum that the energy analysis of §4 hinges upon. In high-density foams the energy analysis selects a unimodal distribution for the values Δ_i, and the total displacement is equally shared by all the cells. In low-density foams, however, the distribution of the values Δ_i is bimodal—whereupon the concept of configurational phases.

For the sake of simplicity, we have focused our discussion of the energetics of heterogeneous solid foam deformation on the simple, but important, case of uniaxially stretched specimens. Two-phase deformation modes are not peculiar to the uniaxial case, however, but rather a common characteristic of compressed open-cell solid foams. Indeed, the strain energy curves accompanying stretch tensors with at least one compressive component are generally nonconvex. (For a tensorial model of solid foams see Wang and Cuitiño 2000). Attaining a better understanding of two-phase deformation modes would be of great interest, in particular for loading cases such as bending and punching, which are prominent among the usual applications of solid foams.

Acknowledgements. We are grateful to the Center for Advanced Food Technology at Rutgers University for their financial support. We also acknowledge General Plastics Manufacturing Company of Tacoma, WA, for the donation of specimens, and thank Mr. Charles Williamson of General Plastics for his kind disposition to all our inquiries.

[3] How many cells it is impossible to ascertain, because the length scale of the microstructure is lost in the process of homogenization. This is related to the lack of uniqueness discussed in §5.

References

- Aref, H. & Vainchtein, D. L. 2000 *Phys. Fluids* **12**, 23–28.
- Artavia, L. D. & Macosko, C. W. 1994 Polyurethane flexible foam formation. In *Low density cellular plastics: Physical basis of behavior*, ed. N. C. Hilyard & A. Cunningham, pp. 22–55. London: Chapman & Hall.
- Böltau, M., Walheim, S., J. Mlynek, J., Krausch, G. & Steiner, U. 1998 *Nature* **391**, 877–879.
- Cahn, J. W. 1961 *Acta Metall.* **9**, 795–801.
- Carr, J. & Pego, R. 1992 *Proc. Roy. Soc. London* A**436**, 569–583.
- de Giorgi, E. 1975 *Rendiconti di Matematica* **8**, 277–294 (in Italian).
- Ericksen, J. L. 1998 *Introduction to the thermodynamics of solids*, 2nd edition, ch. 3. New York: Springer-Verlag.
- Gibson, L. J. & Ashby, M. F. 1997 *Cellular solids*, 2nd edition, ch. 5. Cambridge: University Press.
- Gioia, G. & Ortiz, M. 1997 *Adv. Appl. Mech.* **33**, 119–192.
- Gioia, G., DeSimone, A., Cuitiño, A. M. & Ortiz, M. 2000 Folding energetics in thin-film diaphragms. TAM Report No. 939, University of Illinois at Urbana-Champaign, USA.
- James, R. D. & Kinderlehrer, D. 1990 *Continuum Mech. Thermodyn.* **2**, 215–239.
- Khachaturyan, A. G. 1983 *Theory of Structural Transformations in Solids.*, ch. 6. New York: J. Willey & Sons.
- Kahn-Jetter, Z. L. & Chu, T. C. 1990 *Exp. Mech.* **30**, 10–16.
- Kohn, R. V. & Müller, S. 1994 *Comm. Pure Appl. Math.* **47**, 405–435.
- Kurauchi, T. Sato, N., Kamigato, O. & Komatsu, N. 1984 *J. Mat. Sci.* **19**, 871–880.
- Modica, L. 1987 *Arch. Rat. Mech. Anal.* **98**, 123–142.
- Orme, C. & Orr, B. G. 1997 *Surf. Rev. Lett.* **4**, 71–105.
- Ortiz, M. & Repetto, E. A. 1999 *J. Mech. Phys. Solids* **47**, 397–462.
- Papka, S. D. & Kyriakides, S. 1994 *J. Mech. Phys. Solids* **42**, 1499–1532.
- Peters, W. H. & Ranson, W. F. 1982 *Opt. Eng.* **21**, 427–431.
- Pipkin, A. C. 1993 Seminar on advanced elasticity. Division of Applied Mathematics, Brown University, USA.
- Shaw, M. C. & Sata, T. 1966 *Int. J. Mech. Sci.* **8**, 469–478.
- Vaz, M. F. & Fortes, M. A. 1993 *J. Mat. Sci. Letters* **12**, 1408–1410.
- Vendroux, G. & Knauss, W. G. 1998 *Exp. Mech.* **38**, 86–92.
- Wang, Y. & Cuitiño, A. M. 2000 *J. Mech. Phys. Solids* **48**, 961–988.
- Zhang, D., Zhang, X., & Cheng, G. 1999 *Exp. Mech.* **39**, 62–65.

List of Recent TAM Reports

No.	Authors	Title	Date
856	Zhou, Z., R. J. Adrian, S. Balachandar, and T. M. Kendall	Mechanisms for generating coherent packets of hairpin vortices in near-wall turbulence—*Bulletin of the American Physical Society* **42**, 2243 (1997)	June 1997
857	Neishtadt, A. I., D. L. Vainshtein, and A. A. Vasiliev	Chaotic advection in a cubic stokes flow—*Physica D* **111**, 227 (1997).	June 1997
858	Weaver, R. L.	Ultrasonics in an aluminum foam—*Ultrasonics* **36**, 435–442 (1998)	July 1997
859	Riahi, D. N.	High gravity convection in a mushy layer during alloy solidification—In *Nonlinear Instability, Chaos and Turbulence*, D. N. Riahi and L. Debnath, eds., **1**, 301–336 (1998)	July 1997
860	Najjar, F. M., and S. Balachandar	Low-frequency unsteadiness in the wake of a normal plate, *Bulletin of the American Physical Society* **42**, 2212 (1997)	Aug. 1997
861	Short, M.	A parabolic linear evolution equation for cellular detonation instability—*Combustion Theory and Modeling* **1**, 313–346 (1997)	Aug. 1997
862	Short, M., and D. S. Stewart	Cellular detonation stability, I: A normal-mode linear analysis—*Journal of Fluid Mechanics* **368**, 229–262 (1998)	Sept. 1997
863	Carranza, F. L., and R. B. Haber	A numerical study of intergranular fracture and oxygen embrittlement in an elastic–viscoplastic solid—*Journal of the Mechanics and Physics of Solids*, **47**, 27–58 (1997)	Oct. 1997
864	Sakakibara, J., and R. J. Adrian	Whole-field measurement of temperature in water using two-color laser-induced fluorescence—*Experiments in Fluids* **26**, 7–15 (1999)	Oct. 1997
865	Riahi, D. N.	Effect of surface corrugation on convection in a three-dimensional finite box of fluid-saturated porous material—*Theoretical and Computational Fluid Dynamics*, 13, 189-208 (1999)	Oct. 1997
866	Baker, C. F., and D. N. Riahi	Three-dimensional flow instabilities during alloy solidification—*Bulletin of the American Physical Society* **41**, 1699 (1998)	Oct. 1997
867	Fried, E.	Introduction (only) to *The Physical and Mathematical Foundations of the Continuum Theory of Evolving Phase Interfaces* (book containing 14 seminal papers dedicated to Morton E. Gurtin), Berlin: Springer-Verlag, in press (1998)	Oct. 1997
868	Folguera, A., and J. G. Harris	Coupled Rayleigh surface waves in a slowly varying elastic waveguide—*Proceedings of the Royal Society of London A* **455**, 917–931 (1998)	Oct. 1997
869	Stewart, D. S.	Detonation shock dynamics: Application for precision cutting of metal with detonation waves	Oct. 1997
870	Shrotriya, P., and N. R. Sottos	Creep and relaxation behavior of woven glass/epoxy substrates for multilayer circuit board applications—*Polymer Composites* **19**, 567–578 (1998)	Nov. 1997
871	Riahi, D. N.	Boundary wave–vortex interaction in channel flow at high Reynolds numbers, *Fluid Dynamics Research* **25**, 129–145 (1999)	Nov. 1997
872	George, W. K., L. Castillo, and M. Wosnik	A theory for turbulent pipe and channel flows—paper presented at *Disquisitiones Mechanicae* (Urbana, Ill., October 1996)	Nov. 1997
873	Aslam, T. D., and D. S. Stewart	Detonation shock dynamics and comparisons with direct numerical simulation—*Combustion Theory and Modeling* **3**, 77–101 (1999)	Dec. 1997
874	Short, M., and A. K. Kapila	Blow-up in semilinear parabolic equations with weak diffusion *Combustion Theory and Modeling* **2**, 283-291 (1998)	Dec. 1997
875	Riahi, D. N.	Analysis and modeling for a turbulent convective plume—*Mathematical and Computer Modeling* **28**, 57–63 (1998)	Jan. 1998
876	Stremler, M. A., and H. Aref	Motion of three point vortices in a periodic parallelogram—*Journal of Fluid Mechanics* **392**, 101-128 (1999)	Feb. 1998
877	Dey, N., K. J. Hsia, and D. F. Socie	On the stress dependence of high-temperature static fatigue life of ceramics	Feb. 1998
878	Brown, E. N., and N. R. Sottos	Thermoelastic properties of plain weave composites for multilayer circuit board applications	Feb. 1998

List of Recent TAM Reports (cont'd)

No.	Authors	Title	Date
879	Riahi, D. N.	On the effect of a corrugated boundary on convective motion—*Journal of Theoretical and Applied Mechanics*, in press (1999)	Feb. 1998
880	Riahi, D. N.	On a turbulent boundary layer flow over a moving wavy wall	Mar. 1998
881	Riahi, D. N.	Vortex formation and stability analysis for shear flows over combined spatially and temporally structured walls—*Mathematical Problems in Engineering* 5, 317–328 (1999)	June 1998
882	Short, M., and D. S. Stewart	The multi-dimensional stability of weak heat release detonations—*Journal of Fluid Mechanics* **382**, 109–135 (1999)	June 1998
883	Fried, E., and M. E. Gurtin	Coherent solid-state phase transitions with atomic diffusion: A thermomechanical treatment—*Journal of Statistical Physics* **95**, 1361–1427 (1999)	June 1998
884	Langford, J. A., and R. D. Moser	Optimal large-eddy simulation formulations for isotropic turbulence—*Journal of Fluid Mechanics* **398**, 321–346 (1999)	July 1998
885	Riahi, D. N.	Boundary-layer theory of magnetohydrodynamic turbulent convection—*Proceedings of the Indian National Academy (Physical Science)* **65A**, 109–116 (1999)	Aug. 1998
886	Riahi, D. N.	Nonlinear thermal instability in spherical shells—in *Nonlinear Instability, Chaos and Turbulence* **2**, 377–402 (1999)	Aug. 1998
887	Riahi, D. N.	Effects of rotation on fully non-axisymmetric chimney convection during alloy solidification—*Journal of Crystal Growth* **204**, 382–394 (1999)	Sept. 1998
888	Fried, E., and S. Sellers	The Debye theory of rotary diffusion	Sept. 1998
889	Short, M., A. K. Kapila, and J. J. Quirk	The hydrodynamic mechanisms of pulsating detonation wave instability—*Proceedings of the Royal Society of London, A* **357**, 3621–3638 (1999)	Sept. 1998
890	Stewart, D. S.	The shock dynamics of multidimensional condensed and gas phase detonations—Proceedings of the 27th International Symposium on Combustion (Boulder, Colo.)	Sept. 1998
891	Kim, K. C., and R. J. Adrian	Very large-scale motion in the outer layer—*Physics of Fluids* **2**, 417–422 (1999)	Oct. 1998
892	Fujisawa, N., and R. J. Adrian	Three-dimensional temperature measurement in turbulent thermal convection by extended range scanning liquid crystal thermometry—*Journal of Visualization* **1**, 355-364 (1999)	Oct. 1998
893	Shen, A. Q., E. Fried, and S. T. Thoroddsen	Is segregation-by-particle-type a generic mechanism underlying finger formation at fronts of flowing granular media?—*Particulate Science and Technology* **17**, 141–148 (1999)	Oct. 1998
894	Shen, A. Q.	Mathematical and analog modeling of lava dome growth	Oct. 1998
895	Buckmaster, J. D., and M. Short	Cellular instabilities, sub-limit structures, and edge-flames in premixed counterflows—*Combustion Theory and Modeling* 3, 199–214 (1999)	Oct. 1998
896	Harris, J. G.	*Elastic waves*—Part of a book to be published by Cambridge University Press	Dec. 1998
897	Paris, A. J., and G. A. Costello	Cord composite cylindrical shells	Dec. 1998
898	Students in TAM 293–294	Thirty-fourth student symposium on engineering mechanics (May 1997), J. W. Phillips, coordinator: Selected senior projects by M. R. Bracki, A. K. Davis, J. A. (Myers) Hommema, and P. D. Pattillo	Dec. 1998
899	Taha, A., and P. Sofronis	A micromechanics approach to the study of hydrogen transport and embrittlement	Jan. 1999
900	Ferney, B. D., and K. J. Hsia	The influence of multiple slip systems on the brittle–ductile transition in silicon—*Materials Science Engineering A* **272**, 422–430 (1999)	Feb. 1999
901	Fried, E., and A. Q. Shen	Supplemental relations at a phase interface across which the velocity and temperature jump	Mar. 1999

List of Recent TAM Reports (cont'd)

No.	Authors	Title	Date
902	Paris, A. J., and G. A. Costello	Cord composite cylindrical shells: Multiple layers of cords at various angles to the shell axis	Apr. 1999
903	Ferney, B. D., M. R. DeVary, K. J. Hsia, and A. Needleman	Oscillatory crack growth in glass—*Scripta Materialia* **41**, 275–281 (1999)	Apr. 1999
904	Fried, E., and S. Sellers	Microforces and the theory of solute transport	Apr. 1999
905	Balachandar, S., J. D. Buckmaster, and M. Short	The generation of axial vorticity in solid-propellant rocket-motor flows	May 1999
906	Aref, H., and D. L. Vainchtein	The equation of state of a foam	May 1999
907	Subramanian, S. J., and P. Sofronis	Modeling of the interaction between densification mechanisms in powder compaction	May 1999
908	Aref, H., and M. A. Stremler	Four-vortex motion with zero total circulation and impulse—*Physics of Fluids* **11**, 3704-3715	May 1999
909	Adrian, R. J., K. T. Christensen, and Z.-C. Liu	On the analysis and interpretation of turbulent velocity fields—*Experiments in Fluids*, in press (1999)	May 1999
910	Fried, E., and S. Sellers	Theory for atomic diffusion on fixed and deformable crystal lattices	June 1999
911	Sofronis, P., and N. Aravas	Hydrogen induced shear localization of the plastic flow in metals and alloys	June 1999
912	Anderson, D. R., D. E. Carlson, and E. Fried	A continuum-mechanical theory for nematic elastomers	June 1999
913	Riahi, D. N.	High Rayleigh number convection in a rotating melt during alloy solidification—*Recent Developments in Crystal Growth Research*, in press (2000)	July 1999
914	Riahi, D. N.	Buoyancy driven flow in a rotating low Prandtl number melt during alloy solidification—*Current Topics in Crystal Growth Research*, in press (2000)	July 1999
915	Adrian, R. J.	On the physical space equation for large-eddy simulation of inhomogeneous turbulence	July 1999
916	Riahi, D. N.	Wave and vortex generation and interaction in turbulent channel flow between wavy boundaries	July 1999
917	Boyland, P. L., M. A. Stremler, and H. Aref	Topological fluid mechanics of point vortex motions	July 1999
918	Riahi, D. N.	Effects of a vertical magnetic field on chimney convection in a mushy layer—*Journal of Crystal Growth*, in press (2000)	Aug. 1999
919	Riahi, D. N.	Boundary mode–vortex interaction in turbulent channel flow over a non-wavy rough wall	Sept. 1999
920	Block, G. I., J. G. Harris, and T. Hayat	Measurement models for ultrasonic nondestructive evaluation	Sept. 1999
921	Zhang, S., and K. J. Hsia	Modeling the fracture of a sandwich structure due to cavitation in a ductile adhesive layer	Sept. 1999
922	Nimmagadda, P. B. R., and P. Sofronis	Leading order asymptotics at sharp fiber corners in creeping-matrix composite materials	Oct. 1999
923	Yoo, S., and D. N. Riahi	Effects of a moving wavy boundary on channel flow instabilities	Nov. 1999
924	Adrian, R. J., C. D. Meinhart, and C. D. Tomkins	Vortex organization in the outer region of the turbulent boundary layer	Nov. 1999

List of Recent TAM Reports (cont'd)

No.	Authors	Title	Date
925	Riahi, D. N., and A. T. Hsui	Finite amplitude thermal convection with variable gravity—*International Journal of Mathematics and Mathematical Sciences*, in press (2000)	Dec. 1999
926	Kwok, W. Y., R. D. Moser, and J. Jiménez	A critical evaluation of the resolution properties of *B*-spline and compact finite difference methods	Feb. 2000
927	Ferry, J. P., and S. Balachandar	A fast Eulerian method for two-phase flow	Feb. 2000
928	Thoroddsen, S. T., and K. Takehara	The coalescence–cascade of a drop	Feb. 2000
929	Liu, Z.-C., R. J. Adrian, and T. J. Hanratty	Large-scale modes of turbulent channel flow: Transport and structure	Feb. 2000
930	Borodai, S. G., and R. D. Moser	The numerical decomposition of turbulent fluctuations in a compressible boundary layer	Mar. 2000
931	Balachandar, S., and F. M. Najjar	Optimal two-dimensional models for wake flows	Mar. 2000
932	Yoon, H. S., K. V. Sharp, D. F. Hill, R. J. Adrian, S. Balachandar, M. Y. Ha, and K. Kar	Integrated experimental and computational approach to simulation of flow in a stirred tank	Mar. 2000
933	Sakakibara, J., Hishida, K., and W. R. C. Phillips	On the vortical structure in a plane impinging jet	Apr. 2000
934	Phillips, W. R. C.	Eulerian space–time correlations in turbulent shear flows	Apr. 2000
935	Hsui, A. T., and D. N. Riahi	Onset of thermal–chemical convection with crystallization within a binary fluid and its geological implications	Apr. 2000
936	Cermelli, P., E. Fried, and S. Sellers	Configurational stress, yield, and flow in rate-independent plasticity	Apr. 2000
937	Adrian, R. J., C. Meneveau, R. D. Moser, and J. J. Riley	Final report on 'Turbulence Measurements for Large-Eddy Simulation' workshop	Apr. 2000
938	Bagchi, P., and S. Balachandar	Linearly varying ambient flow past a sphere at finite Reynolds number—Part 1: Wake structure and forces in steady straining flow	Apr. 2000
939	Gioia, G., A. DeSimone, M. Ortiz, and A. M. Cuitiño	Folding energetics in thin-film diaphragms	Apr. 2000
940	Chaïeb, S., and G. H. McKinley	Mixing immiscible fluids: Drainage induced cusp formation	May 2000
941	Thoroddsen, S. T., and A. Q. Shen	Granular jets	May 2000
942	Riahi, D. N.	Non-axisymmetric chimney convection in a mushy layer under a high-gravity environment	May 2000
943	Christensen, K. T., S. M. Soloff, and R. J. Adrian	PIV Sleuth: Integrated particle image velocimetry interrogation/validation software	May 2000
944	Wang, J., N. R. Sottos, and R. L. Weaver	Laser induced thin film spallation	May 2000
945	Riahi, D. N.	Magnetohydrodynamic effects in high gravity convection during alloy solidification	June 2000
946	Gioia, G., Y. Wang, and A. M. Cuitiño	The energetics of heterogeneous deformation in open-cell solid foams	June 2000